18

Reduced-Order Simulation

In chapter 17 we discussed various techniques for reduced-order modeling of microsystems. In this chapter, we discuss the application of these techniques to several examples in microflows. First, we present circuit and device models and their application to lab-on-a-chip systems. Then, we discuss macromodeling of squeeze film damping by applying equivalent circuit, Galerkin, mixed-level, and black box models. Next, we present a compact model for electrowetting. Finally, we summarize some of the software packages that are available for reduced-order simulation.

18.1 Circuit and Device Models for Lab-on-a-Chip Systems

The concept of a micro-total analysis system (μ-TAS) or a lab-on-a-chip for integrated chemical and biochemical analysis has grown considerably in scope since its introduction (Manz et al., 1990; Reyes et al., 2002). μ-TAS involves the miniaturization of all the functions found in chemical analysis, including fluidic transport, mixing, reaction, and separation (Greenwood and Greenway, 2002), so that the entire chemical measurement laboratory could be miniaturized onto a device of a few square centimeters. For example, the system shown in Figure 18.1 incorporates the essential processes (fluidic transport, mixing, reaction, and separation) involved in a μ-TAS. One of the critical elements of any microfluidic system or μ-TAS is its fluidic transport system. For the example considered in Figure 18.1, the fluid

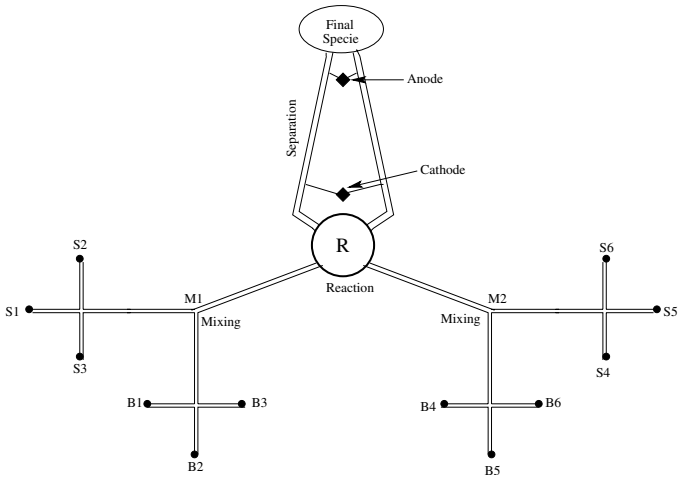

FIGURE 18.1. A prototype chemical analysis system. The system incorporates fluidic transport, mixing, reaction, and separation.

is transported from the ends of the cross-shaped segments to the reservoir marked as the "Final Species." Most microfluidic chips transport the fluid electrokinetically (see Chapter 7) and/or by pressure. Electrokinetic transport and control of fluids has the advantage that it eliminates the need for mechanically moving parts, such as valves and pumps, which have thus far been difficult to construct and interface to microchip systems (Weigl et al., 2003).

An important element of the μ-TAS is the reaction chamber. As shown in Figure 18.1, chemical/biological species are transported to the reaction chambers, where chemical reactions take place leading to the formation of a product. The rate of formation of the product is dependent on the flux of the reactant, the proportion of the various reactants in the solution, the order of the reaction, and the reaction kinetics. The solution from the reaction chamber is sometimes tapped for detection. The detection of the product is typically easier than the detection of the reacting species. In such a case, the presence of the product and the concentration of the product can give quantitative information about the reacting species. Thus, often reaction and detection schemes are intrinsically linked together, and both of these form an integral part of the μ-TAS.

Another important functionality in μ-TAS is the separation of biomolecules and biochemical species. Electrophoresis and isoelectric focusing (see Chapter 7 for details) are the most commonly employed methods of separation. In Figure 18.1, for example, the separation is based on electrophoresis. Higher field intensity is generally tolerable for electrophoretic separation in microchannels (Ehrfeld, 2003). Smaller characteristic dimensions in combi-

nation with higher field intensities lead to a shorter time scale of separation, which is a fundamental advantage in μ-TAS compared to macroscopic devices.

When designing integrated microfluidic systems of the type shown in Figure 18.1, some important objectives are to:

1. Increase the throughput.
2. Improve the homogeneity of the mixture.
3. Obtain higher separation efficiency.
4. Perform detection faster.

However, it may not be possible to attain all these objectives, and there can be a trade-off leading to an optimized design. In this section, using the techniques discussed in Chapter 17, "easy-to-use" circuit and device models are presented, which can be used to explore the design space and select an optimal design for integrated microfluidic systems to perform various functions. The model development is illustrated using the example shown in Figure 18.1. The models are, however, general enough that they can be applied or extended to other microfluidic systems. The development of a compact/circuit model for fluid flow due to a combined pressure and electrical potential gradient is first discussed. The compact model is described in two parts, namely, the electrical model and the fluidic model.

18.1.1 Electrical Model

For microfluidic devices that rely on the electrokinetic force as the driving force, the electric field must be computed first. In the case of electroosmotic flow (see Chapter 7 for details; here we restate only the essential equations to derive the circuit models), the potential field due to an applied potential can be computed by solving the Laplace equation:

$$\nabla^2 \phi = 0, \tag{18.1}$$

where ϕ is the electrical potential. Since equation (18.1) predicts a linear potential drop for simple straight channels, the potential variation can be represented by linear electrical resistances. In order to develop a complete circuit that takes into account the charge stored in the electrical double layer (EDL), capacitive elements also need to be included in modeling the electrical domain. The EDL can be decomposed into the stern layer and the diffuse layer. As the stern layer and the diffuse layer store charge, the capacitance associated with these layers is important. In addition, the capacitance of the channel wall, which arises due to a potential difference across the channel wall, needs to be taken into account. The electrical resistance of the EDL can be safely neglected, since the effective resistance

of the EDL is much higher than the resistance of the channel filled with buffer (Hayes and Ewing, 2000). Figure 18.2(a) and Figure 18.2(b) illustrate a typical cross-shaped channel segment (this is similar to the cross shapes formed by S1, S2, M1, S3 or B1, B2, B3, M1 or B4, B5, B6, M2 or S4, S5, S6, M2 in Figure 18.1) in a microfluidic system and its circuit representation, respectively.

The electrical resistance of a solution-filled simple straight channel is given by the expression

$$R_{ch,i} = \frac{\rho_{\text{sol},i} L_i}{A_{c,i}},$$

where $\rho_{\text{sol},i}$ is the electrical resistivity of the solution in the ith channel, $i = 1, 2, \ldots 4$ (see Figure 18.2(b)), L_i is the length of the ith channel, $A_{c,i}$ is the cross-sectional area of the ith channel, and $R_{\text{ch},i}$ is the electrical resistance of the ith channel.

The expression for the *effective capacitance*, shown in Figure 18.2(b), is given by

$$(C_{\text{eff},i})^{-1} = (C_{\text{st},i})^{-1} + (C_{\text{dl},i})^{-1} + (C_{\text{wall},i})^{-1},$$

where $C_{\text{st},i}$ is the capacitance of the stern layer of the ith channel, $C_{\text{dl},i}$ is the capacitance of the diffuse layer of the ith channel, and $C_{\text{wall},i}$ is the capacitance of the ith channel wall; $C_{\text{st},i}$ is given by the expression (Oldham and Myland, 1994)

$$C_{\text{st},i} = \frac{\epsilon A_{s,i}}{x_{H,i}},$$

where ϵ is the permittivity of the fluid in the channel, $A_{s,i}$ is the inner surface area of the ith channel, and $x_{H,i}$ is the thickness of the stern layer. The *capacitance of the diffuse layer*, $C_{\text{dl},i}$, is given by the expression (Davies and Rideal, 1966)

$$C_{\text{dl},i} = \frac{\sigma_{T,i} A_{s,i}}{\left\{ \left(\frac{2k_{\text{B}}T}{ze} \right) \sinh^{-1} \left(\frac{\sigma_{T,i}}{c^{\frac{1}{2}}} \left[\frac{500\pi}{\epsilon RT} \right]^{\frac{1}{2}} \right) \right\}},$$

where $\sigma_{T,i}$ is the intrinsic surface charge density on the channel wall, k_{B} is Boltzman's constant, T is the temperature, z is the valence of the counterion, e is the charge of an electron, c is the concentration of the counterion in the bulk solution, and R is the universal gas constant. The *capacitance of the wall* for a cylindrical channel, $C_{\text{wall},i}$, is given by the expression

$$C_{\text{wall},i} = \frac{\epsilon A_{s,i}}{r_i \ln(\frac{r_o}{r_i})},$$

where r_i is the inner radius of the channel and r_o is the outer radius of the channel.

When no potential difference is applied across the channel wall, no charge is induced in the channel wall. As a result, the capacitance of the channel wall can be neglected in the computation of the effective capacitance.

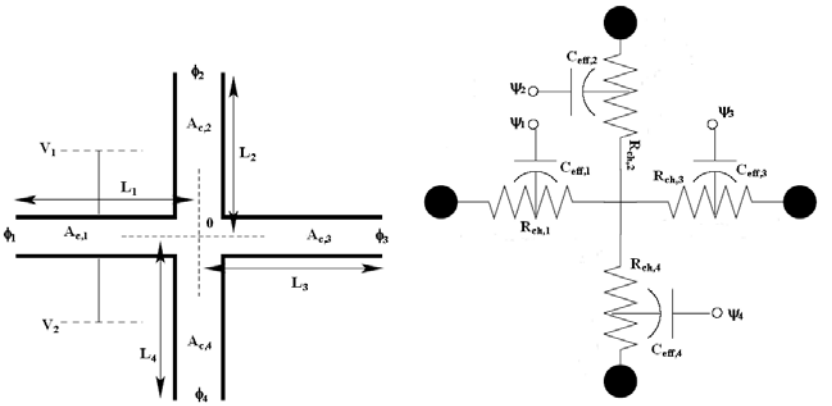

(a) (b)

FIGURE 18.2. (a) A typical cross-shaped channel segment of a microfluidic system. The electrical potentials, ϕ_{1-4}, are given. V_1 and V_2 are the transverse applied potentials. (b) The electrical network representation for the cross-shaped channel. $R_{\mathrm{ch},1-4}$ are the electrical resistances, ψ_{1-4} are the surface potentials of the channel walls, and $C_{\mathrm{eff},1-4}$ are the capacitances of the EDLs.

For example, there is no wall capacitance for $i = 2, 3, 4$, since there is no applied voltage across the channel, as shown in Figure 18.2(a). Typically, the capacitance of the stern layer is much higher than the capacitance of the diffuse layer (Oldham and Myland, 1994). Also, when capacitances are connected in series (as in this case), the capacitance with the smaller value dominates. Therefore, in most cases the effective capacitance, C_{eff}, can be approximated by the diffuse layer capacitance, C_{dl}. The effective capacitance can be related to the surface potential by the expression

$$C_{\mathrm{eff},i}\psi_{0,i} = q_{st,i} = \sigma_{T,i}A_{s,i},$$

or

$$\psi_{0,i} = \frac{\sigma_{T,i}A_{s,i}}{C_{\mathrm{eff},i}}, \tag{18.2}$$

where $\psi_{0,i}$ is the surface potential on the ith channel and $q_{\mathrm{st},i}$ is the total charge stored in the EDL of the ith channel.

18.1.2 Fluidic Model

For the fluidic transport driven by an electrical field and/or a pressure gradient, the "through quantities" are the flow rates through the channels, while the "across quantities" are the electrical potential differences and the pressure differences imposed on the fluidic channels. In this section we present a derivation of the constitutive equation relating the "through

quantities" to the "across quantities" making use of the continuity equation and the steady-state momentum equation for electroosmotic flows (see Chapter 7 for details).

Slip Case

The slip case model can be used when the thickness of the EDL is insignificant compared to the depth or diameter of the channel. The body force, $\mathbf{F} = \rho_e \mathbf{E}$ (see Chapter 7), is nonzero only within a few Debye lengths from the channel wall, since the potential induced by the zeta potential drops to zero very quickly near the channel wall (Mitchell et al., 2000). In the development of the compact model for the slip flow case, we will assume that the flow is fully developed and the thickness of the EDL is insignificant compared to the thickness or diameter of the channel (this assumption usually holds good for channels larger than 200 nm; see Chapter 7 for details). As a result, the effect of the electrokinetic force can be represented by a slip velocity at the wall given by the Helmholtz–Smoluchowski equation (see section 7.3)

$$u_p = -\frac{\epsilon\zeta}{\mu}\nabla\phi, \tag{18.3}$$

where $\nabla\phi$ is the potential gradient across the fluidic channel and ζ is the zeta potential of the fluidic channel. The Poisson–Boltzmann equation, which is used for the full-scale simulation of electroosmotic flow, can be linearized for low values of surface charge density. Then, the Debye–Hückel theory predicts the following relationship between the zeta potential, ζ, and the surface potential, ψ_0 :

$$\zeta = \psi_0 \exp(-\kappa\chi),$$

where κ is the inverse of the Debye length and χ is the radius of the counterion. The surface potential can be computed from equation (18.2) using the capacitance model. Thus, from knowing the surface potential, the zeta potential of the channel wall can be computed. The velocity profile across a capillary slit is a function of only the slip velocity and the pressure gradient, i.e.,

$$u = -\frac{1}{2\mu}\frac{dp}{dx}\left(y^2 - \frac{h^2}{4}\right) + u_p, \tag{18.4}$$

where x denotes the stream direction of the channel, y denotes the transverse direction of the channel, and h is the channel depth. Since u_p is given by equation (18.3), solving for the velocity in equation (18.4) is reduced to computing the pressure distribution in the fluidic network. By taking divergence of the momentum equation and applying the continuity condition, we get the expression

$$\nabla^2 p = \nabla \cdot \mathbf{F} - \nabla \cdot (\rho_f(\mathbf{u} \cdot \nabla)\mathbf{u}).$$

In the regions where the flow is fully developed, the convection term $(\mathbf{u}\cdot\nabla)\mathbf{u}$ is zero. Thus, $\nabla\cdot(\rho_f(\mathbf{u}\cdot\nabla)\mathbf{u})$ vanishes. The term corresponding to the divergence of the force must be zero in the fully developed flow regions; otherwise, the flow would not be fully developed due to the nonuniform body force. Hence, for the region where the flow is fully developed, the pressure calculation is reduced to a Laplace equation,

$$\nabla^2 p = 0. \tag{18.5}$$

Thus, equation (18.5) decouples the solution of pressure from the solution of velocity.

Integrating the velocity profile given in equation (18.4) across the cross-section of the capillary slit and using equations (18.1), (18.3), and (18.5), we get the following expression for the flowrate per unit width:

$$Q = \left(\frac{h^3}{12\mu L}\right)\Delta p + \left(\frac{\epsilon\zeta h}{\mu L}\right)\Delta\phi. \tag{18.6}$$

For the ith channel in an array of channels, equation (18.6) can be rewritten as:

$$Q_i = H_i\Delta p_i + E_i\Delta\phi_i, \tag{18.7}$$

where H_i is the hydraulic conductance of the ith channel, E_i is the electrohydraulic conductance of the ith channel, Δp_i is the pressure drop in the ith channel, and $\Delta\phi_i$ is the electrical potential drop in the ith channel. The expressions for H_i and E_i for the capillary slit are given in equation (18.6). For a cylindrical channel, the hydraulic conductance and the electro-hydraulic conductance are given by

$$H_i = \frac{\pi {r_i}^4}{8\mu_i L_i} \qquad \text{and} \qquad E_i = \frac{\epsilon\zeta_i\pi {r_i}^4}{\mu_i L_i},$$

where r_i is the inner radius of the ith cylindrical channel. Equation (18.7) is the constitutive relationship, which relates the "through quantity" to the "across quantities" (a combined pressure and electrical potential drop). If the flow is driven by only a pressure gradient, then the second term in equation (18.6) can be neglected. Similarly, if the flow is driven by only an electric field, then the first term on the right-hand side of equation (18.6) can be neglected. Figure 18.4 shows the circuit representations of the fluidic domain for the cross-shaped channel segment shown in Figure 18.3. It is to be noted that the total flow is the sum of the electrokinetically driven flow and the pressure-driven flow.

No-Slip Case

The slip velocity model discussed above can be employed when the Debye length is thin compared to the channel width. However, when the Debye

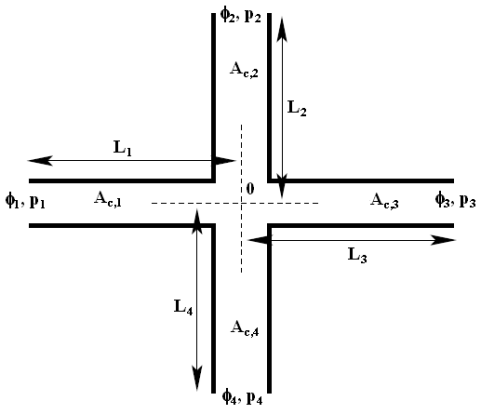

FIGURE 18.3. A cross-shaped channel with a combined pressure and electrical potential gradients. The electrical potentials, ϕ_{1-4}, and pressures, p_{1-4}, are given.

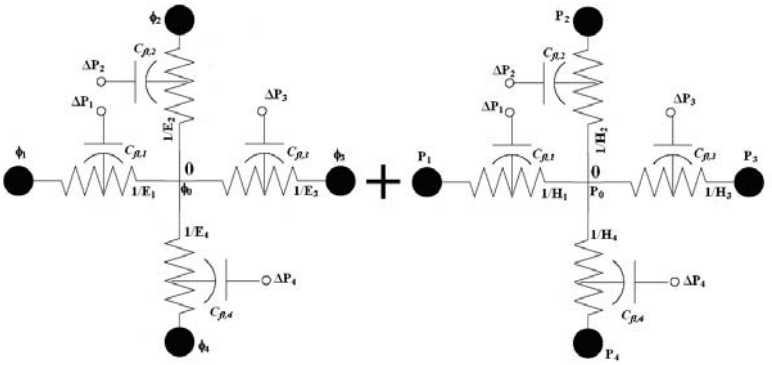

FIGURE 18.4. Circuit representation for the electrokinetically driven flow is on the left. E_{1-4} are the electrohydraulic conductances of the channels and $(C_{\mathrm{fl},1-4})$ are the fluidic capacitances. Circuit representation for the pressure-driven flow is given on the right. H_{1-4} are the hydraulic conductances of the channels. The plus sign between the two figures indicates that the total flow is the sum of the electrokinetically driven flow *and* the pressure-driven flow.

length is comparable to the channel width, the slip velocity model may not be accurate. For a capillary slit, the velocity profile is given by the expression (Patankar and Hu, 1998; Keh and Tseng, 2001)

$$u_{(y)} = -\frac{1}{2\mu}\frac{dp}{dx}\left(y^2 - \frac{h^2}{4}\right) - \frac{\epsilon}{\mu}\nabla\phi\left(\psi_0 - \psi_{(y)}\right), \tag{18.8}$$

where

$$\psi_{(y)} = \frac{\psi_0 \cosh(\frac{y}{\lambda_D})}{\cosh(\frac{h}{\lambda_D})}, \tag{18.9}$$

and λ_D is the Debye length; see equation (7.1). Integrating the velocity profile (given in equation (18.8)) across the cross-section and using equation (18.9), we get the following expressions for the hydraulic conductance and the electrohydraulic conductance of the ith channel:

$$H_i = \frac{{h_i}^3}{12\mu_i L_i} \quad \text{and} \quad E_i = \frac{\epsilon}{\mu_i L_i}\psi_0 \left(2h_i - 2\lambda_D \frac{\sinh\left(\frac{h_i}{\lambda_D}\right)}{\cosh\left(\frac{h_i}{\lambda_D}\right)}\right).$$

Fluidic Channels with Elastic Membranes

In the case of channels with integrated elastic parts in them (e.g., a flexible membrane) a capacitive element needs to be included in the circuit model of the fluidic domain as shown in Figure 18.4. The fluidic capacitor can be modeled as

$$C_{\text{fl}} = \frac{\iint_\Gamma w(x,y)d\Gamma}{p}, \tag{18.10}$$

where C_{fl} is the fluidic capacitance, w is the deflection, Γ is the total surface area of the flexible membrane, and p is the pressure difference across the channel wall. For a rectangular membrane of dimensions $a \times b$, the fluidic capacitance from equation (18.10) is given by

$$C_{fl} = \frac{4a}{\pi^5 D_r} \sum_{m=1,3,5,\ldots}^{\infty} \frac{(-1)^{\frac{m-1}{2}}}{m^5} \frac{\sin(\frac{m\pi}{2})}{\frac{m\pi}{a}} \left\{\frac{b}{2} + \frac{a}{2m\pi}[\alpha_m - \tanh(\alpha_m)(3 + \alpha_m \tanh(\alpha_m))]\right\},$$

where

$$\alpha_m = \frac{m\pi b}{2a},$$

and D_r is the rigidity of the membrane given by

$$D_r = \frac{E_{\text{mod}} h_m^3}{12(1-\nu^2)},$$

where h_m is the thickness of the membrane, E_{mod} is the elastic modulus of the membrane, and ν is the Poisson ratio of the membrane.

The implementation of the electrical model and the fluidic model is carried out using the *modified nodal analysis* technique (Ogrodzki, 1994). Once the variations of ϕ and p are known, the flowrate in each channel can be computed using the constitutive relationship given in equation (18.7).

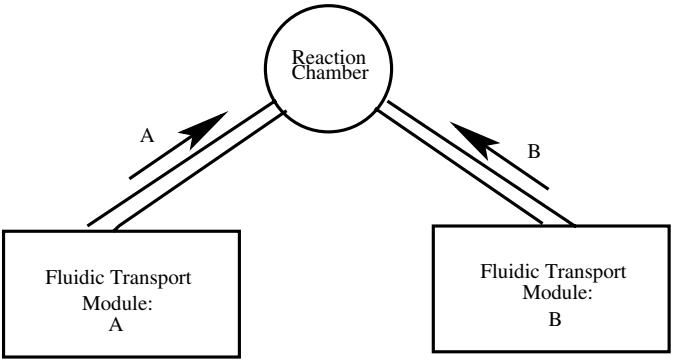

FIGURE 18.5. Chemical species A and B are transported to the reaction chamber, where they undergo a second-order reversible reaction process.

18.1.3 Chemical Reactions: Device Models

Consider a scheme (shown in Figure 18.5) in which the chemical species A and B are transported to the reaction chamber, where they undergo a second-order reversible reaction process to produce species C. The governing equations for this reaction process are given by

$$
\begin{aligned}
&A + B \underset{k_2}{\overset{k_1}{\rightleftharpoons}} C, \\
&\frac{\partial m_A}{\partial t} = Q_A C_A - k_1(m_A)(m_B) + k_2(m_C), \\
&\frac{\partial m_B}{\partial t} = Q_B C_B - k_1(m_A)(m_B) + k_2(m_C), \\
&\frac{\partial m_C}{\partial t} = k_1(m_A)(m_B) - k_2(m_C),
\end{aligned}
$$

where Q_i is the flowrate of the ith species, which is computed from the fluidic transport model (or known from the design specifications), C_i is the concentration of the ith species, m_i is the number of moles of the ith species present in the reaction chamber, k_1 is the forward reaction rate, and k_2 is the backward reaction rate. A trapezoidal scheme is used to discretize the ODEs given above. The discretized equations are given by

$$
\begin{aligned}
\frac{(m_A^{n+1} - m_A^n)}{\Delta t} &= Q_A C_A - \frac{k_1}{4}(m_A^{n+1} + m_A^n)(m_B^{n+1} + m_B^n) + \frac{k_2}{2}(m_C^{n+1} + m_C^n), \\
\frac{(m_B^{n+1} - m_B^n)}{\Delta t} &= Q_B C_B - \frac{k_1}{4}(m_A^{n+1} + m_A^n)(m_B^{n+1} + m_B^n) + \frac{k_2}{2}(m_C^{n+1} + m_C^n), \\
\frac{(m_C^{n+1} - m_C^n)}{\Delta t} &= \frac{k_1}{4}(m_A^{n+1} + m_A^n)(m_B^{n+1} + m_B^n) - \frac{k_2}{2}(m_C^{n+1} + m_C^n).
\end{aligned}
$$

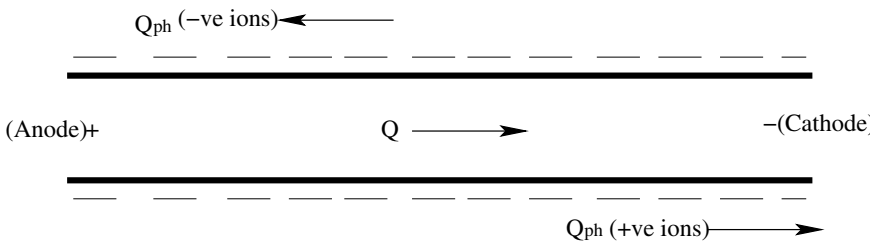

FIGURE 18.6. A basic separation unit, which can separate species that are oppositely charged, have different valences or different electrophoretic mobilities.

The nonlinear equations given above are solved by employing a Newton–Raphson scheme to compute m_A^{n+1}, m_B^{n+1} and m_C^{n+1} at the $(n+1)$th time step given m_A^n, m_B^n, and m_C^n at the nth time step. These equations constitute the device model for the reaction module.

18.1.4 Separation: Device Model

Figure 18.6 shows a simple separation mechanism, which is repeated as the basic unit in the circular separation device reported in (Kutter, 2000). The separation unit can separate species that are either oppositely charged or have different valences or different electrophoretic mobilities. The total flux of a given species through a channel is given by the following expression:

$$J_t = \left[D_{\text{diff}} \frac{\partial c}{\partial x} + \frac{z F_c D_{\text{diff}}}{RT} (\nabla \phi)\, c + v_{\text{conv}} c \right] A_c, \tag{18.11}$$

where J_t is the total flux, D_{diff} is the diffusion coefficient of the species, c is the concentration of the species, F_c is Faraday's constant, z is the valence of the ion, R is the universal gas constant, T is the temperature, A_c is the cross-sectional area of the fluidic channel, and v_{conv} is the convective velocity of the flow that arises due to the bulk flowrate, Q, given in equation (18.6):

$$v_{\text{conv}} = \frac{Q}{A_c}.$$

From equation (18.11), the total flux is the sum of the diffusive flux (given by the first term), the electrophoretic flux (given by the second term and it is zero for uncharged species), and the convective flux (given by the last term), which arises due to the bulk flow in the channel. Typically, the separation unit is designed in such a way that the convective flux and the electrophoretic flux (for charged species) dominate over the diffusive flux (Fletcher et al., 1999). Thus, assuming that the diffusive flux is negligible,

the expression for the total flux is given by

$$J_t = \left[\frac{zF_c D_{\text{diff}}}{RT} (\nabla \phi)\, c + v_{\text{conv}} c \right] A_c$$

or

$$J_t = (Q_{\text{ph}} + Q)c,$$

where Q is the convective flowrate, which is computed using equation (18.6), and Q_{ph} is the electrophoretic flow rate, which is given by the expression (Fletcher et al., 1999)

$$Q_{\text{ph}} = \left(\frac{zF_c D_{\text{diff}}}{RT} \right) A_c \nabla \phi.$$

Thus, the constitutive equation, which relates the "through quantity" (electrophoretic flowrate) to the "across quantity" (electrical potential difference), in the case of electrophoretic flow, is given by

$$Q_{ph} = \left(\frac{zF_c D_{\text{diff}} A_c}{RTL} \right) \Delta \phi = \mathcal{F} \Delta \phi,$$

where $\mathcal{F}$ is the electrophoretic conductance of the fluidic channel.

Consider an example, where two species A and B are present in the separation channel shown in Figure 18.6. Assume that species A is unit-positively charged and species B is unit-negatively charged, while the surface of the channel has a negative fixed charge. Therefore, the electroosmotic flow through the channel would be from left to right (i.e., from the anode side to the cathode side) as shown in Figure 18.6. The electrophoretic flow for A would be from left to right, but that for B would be in the opposite direction. This is due to the difference in the electrophoretic velocities of these two species. Thus, the ratio of the rate of molar increment at the outlet of the separation channel for the two species is given by the expression

$$\textit{Separation Ratio} = \frac{(Q + \text{sign}(z_A) \times \mid Q_{\text{ph}} \mid_A) c_A^{\text{in}}}{(Q + \text{sign}(z_B) \times \mid Q_{\text{ph}} \mid_B) c_B^{\text{in}}} = \frac{(Q + \mid Q_{\text{ph}} \mid_A) c_A^{\text{in}}}{(Q - \mid Q_{\text{ph}} \mid_B) c_B^{\text{in}}},$$

where c_A^{in} is the concentration of species A at the inlet, and c_B^{in} is the concentration of species B at the inlet. Considering that the bulk flow is due to electrical potential gradient only (i.e., pressure-driven flow is absent), the separation ratio of the species can be expressed in terms of the electrophoretic conductance, electrohydraulic conductance, and the inlet concentration of the species, i.e.,

$$\textit{Separation Ratio} = \frac{(H + \mathcal{F}_A) c_A^{\text{in}}}{(H + \mathcal{F}_B) c_B^{\text{in}}}. \tag{18.12}$$

Thus, the knowledge of the electrophoretic conductance and the electrohydraulic conductance can be used to compute the separation ratio using equation (18.12), which can be considered as the device model for the separation module.

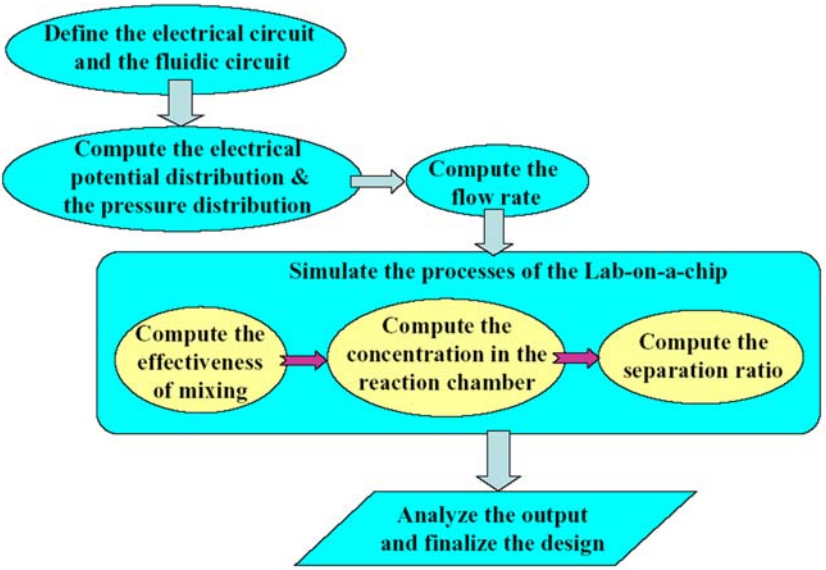

FIGURE 18.7. A block diagram for combined circuit/device analysis of the lab-on-a-chip system shown in Figure 18.1.

18.1.5 Integration of the Models

Figure 18.7 summarizes the integration of the circuit and device models for the prototype integrated microfluidic system shown in Figure 18.1. The circuit-based electrical model is first employed to compute the electrical potential distribution in the entire microfluidic system. Using the electrical potential distribution as an input, the fluidic circuit model is used to compute the flow variables (the pressure distribution, flowrate, etc.) in the entire system. The flowrates through various channels are then used to compute the mixing ratio/efficiency, reactions and the separation ratio. Even though Figure 18.7 is specific to the microfluidic system shown in Figure 18.1, it can be generalized to various other microfluidic systems by appropriately combining the electrical, fluidic, mixing, reaction/detection, and separation modules.

18.1.6 Examples

In this section, we demonstrate the application of the models and the implementation using several examples. In the first example (Figure 18.8, (Jacobson et al., 1999)), we consider microfluidic devices, which can be used for electrokinetically driven parallel and serial mixing. In the second

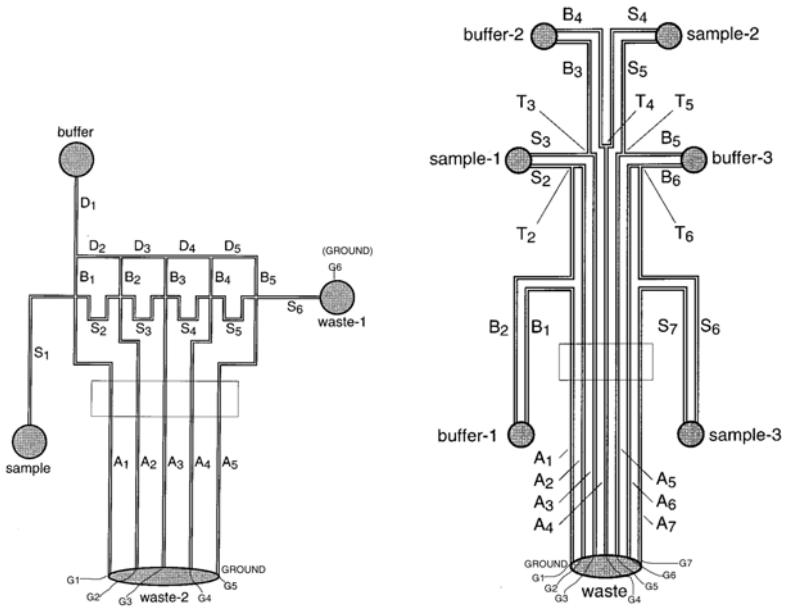

FIGURE 18.8. Schematics of the microchips for parallel (a) and serial (b) electrokinetic mixing. The circles depict sample, buffer, and waste reservoirs. The sample, buffer, and analysis channels are labeled "S," "B," and "A," respectively. The T intersections are the basic units for the parallel mixing device, while the cross intersections are the basic units for the serial mixing device (Jacobson et al., 1999).

example, we demonstrate a circuit-model-based analysis of a pneumatically controlled fluidic transport system, which has been used in a high-density microfluidic chip by (Thorsen et al., 2002). In the final example, we consider an integrated system, and a complete simulation-based analysis of the lab-on-a-chip.

Electrokinetically Driven Mixing

Microfluidic devices for parallel and serial mixing have been experimentally demonstrated (Jacobson et al., 1999). The parallel mixing device (Figure 18.8a) is designed with a series of independent T-intersections, and the serial mixing device (Figure 18.8b) is based on an array of cross-intersections. Figures 18.9(a) and 18.9(b) show the circuit representation of the mixing devices. Since the channels do not contain any flexible walls, the fluidic capacitances are neglected. The parameters (e.g., channel dimensions and applied potential) used in the simulation are the same as those used in the experiments reported in (Jacobson et al., 1999). The zeta

potential of the channel walls for this example is computed from the capacitor model and has been verified with the experimental results given in (Jacobson et al., 1999). The expressions that have been used to compute the sample fraction are the same as those given in (Jacobson et al., 1999). For the parallel mixing device, the sample fraction in the jth analysis channel is computed by the expression

$$(\text{S.F.})_{A_j} = (n)_{A_j} = \frac{(Q)_{S_j}}{(Q)_{A_j}},$$

where S.F. is the sample fraction, $(Q)_{S_j}$ is the flowrate of the sample in the jth analysis channel, and $(Q)_{A_j}$ is the flowrate of the total solution in the jth analysis channel. For the serial mixing device, the sample fraction in the $(m+1)$th analysis channel is computed by the expression

$$(\text{S.F.})_{A_{m+1}} = (n)_{A_{m+1}} = \prod_{k=1}^{m} \left[1 - \frac{(Q)_{B_k}}{(Q)_{S_{k+1}}}\right],$$

where $(Q)_{B_k}$ is the flowrate of the buffer in the kth channel and $(Q)_{S_{k+1}}$ is the sample flowrate in the $(k+1)$th channel. Table 18.1 gives a comparison of the simulated and experimental results for the parallel and serial mixing devices. The simulation results show very good agreement with the experimental results. The CPU times to compute the electrical variables and the fluidic variables for the systems shown in Figure 18.8 (i.e., the mixing devices) were of order 1 second on a 800-MHz PC. Figures 18.10a and 18.10b show the variation in the sample fraction that can be obtained by controlling the electrical potential at the buffer and the sample reservoirs. These results demonstrate the advantage of the circuit model for designing microfluidic systems. It is practically impossible to get the variation of the output parameter with the input parameter varying over such a large range using experimental techniques or full-scale simulation methods.

The depth of the channels considered for parallel and serial mixing are 10 μm and 5.5 μm, respectively. For such large depths, the slip flow circuit model presented in Section 18.1.2 gives accurate results. Even if a no-slip flow circuit model is employed, the results would match exactly with the slip flow circuit model. However, as the depth of the channel gets smaller, the no-slip model can produce more accurate results than the slip-flow model. Shown in Figure 18.11 is a comparison of the relative error between the full simulation results and the slip and no-slip models for channel depths of 50 nm, 100 nm, and 200 nm. The Debye length is 10 nm in all cases. For both models, the error grows as the depth of the channel decreases. However, the error is much smaller with the no-slip model than with the slip model. Also, the rate of growth of the error is smaller with the no-slip model than with the slip model.

TABLE 18.1. A comparison of the simulated and experimental results for different types of mixing.

CHANNEL (PARALLEL MIXING)	SAMPLE FRACTION (EXPERIMENT)	SAMPLE FRACTION (SIMULATION)
A_1	0	0
A_2	0.84	0.833
A_3	0.67	0.675
A_4	0.51	0.522
A_5	0.36	0.340
A_6	0.19	0.165
A_7	1.0	1.0
CHANNEL (SERIAL MIXING)	SAMPLE FRACTION (EXPERIMENT)	SAMPLE FRACTION (SIMULATION)
A_1	1.0	1.0
A_2	0.36	0.37
A_3	0.21	0.22
A_4	0.12	0.12
A_5	0.059	0.053

Large-Scale Integration

In Chapter 1, we discussed a large-scale-integration-based microfluidic chip in Figure 1.31. Here we revisit the problem and show some results obtained using the circuit models discussed in the previous chapter. In the example shown in Figure 1.31, the fluidic transport system consists of two layers (Figure 18.12): the "control" layer, which contains all channels required to actuate the valves, is situated on top of the "flow" layer, and the "flow" layer contains the network of the channels being controlled (Unger et al., 2000). All biological assays and fluid manipulations are performed in the

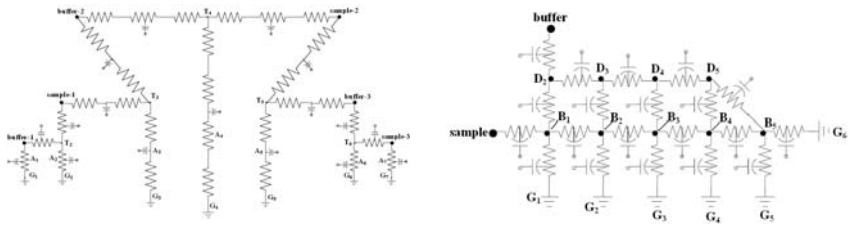

FIGURE 18.9. (a) The circuit (both fluidic and electrical) representation of the parallel mixing device. Since the flow is electrokinetically driven, the fluidic resistance of the channel is the inverse of the electrohydraulic conductance. (b) The circuit representation of the serial mixing device.

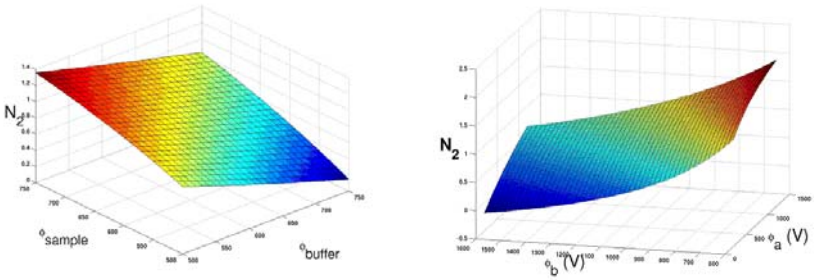

(a) Parallel mixing (b) Serial mixing

FIGURE 18.10. Variation in the sample fraction (denoted by N_2) of the second analysis channel when the applied potential (in "volts") in the sample reservoir and the buffer reservoir is changed. The plots for the other analysis channels (in both cases) have the same pattern.

flow layer. A valve is created whenever a control channel crosses a flow channel (Figure 18.12). The resulting thin membrane at the junction between the two channels can be deflected by fluidic actuation (Thorsen et al., 2002; Unger et al., 2000).

The schematic A of Figure 18.12 shows the orientation of the control layer and the flow layer. The schematic B of Figure 18.12 shows the valve closing for rectangular and rounded channels. The dotted lines indicate the contour of the top of the channel for a rectangular (left) and a rounded (right) channel as pressure is increased. In the example shown in Figure 18.13(a), rectangular channels are considered. Making multiple, independently actuated valves in a device requires independent control of the pressure applied to each control line. Figure 18.13(a) shows an example of such a device. From the "top view," the black channels oriented from west to east are

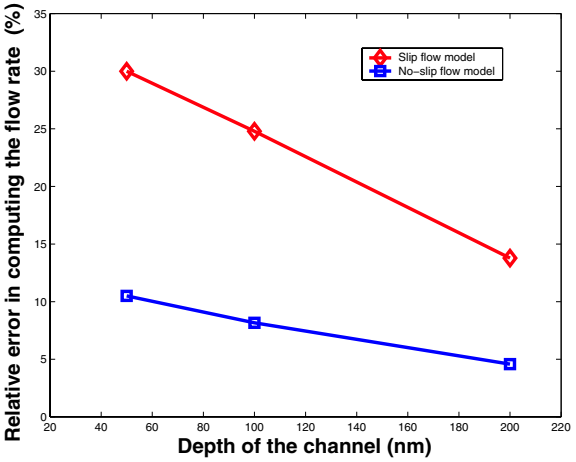

FIGURE 18.11. A comparison of the percentage relative error in the bulk flowrate Q between the slip flow model and the no-slip flow model, when compared with full-scale simulation.

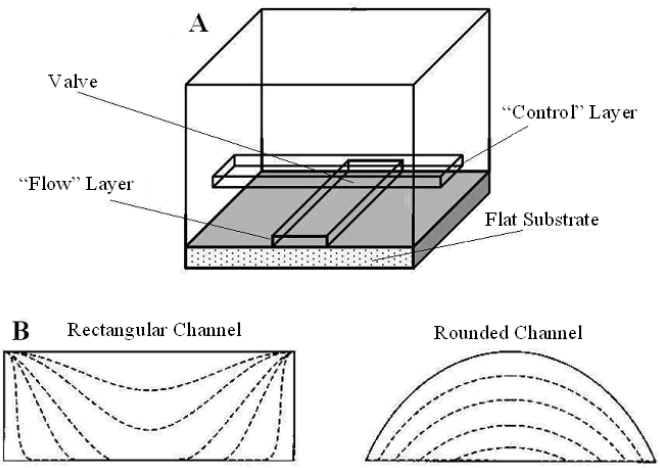

FIGURE 18.12. (A) Schematic of the arrangement of the control layer and the flow layer used for attaining pneumatic control. (B) Schematic of the valve closing for rectangular and rounded channel (Unger et al., 2000).

the control channels, and the gray channels oriented from north to south are flow channels. The control layer is on top of the flow layer. The flow channels are numbered from 0 to 7, and the control channels are named in alphabetic order from A to F. A valve at the intersection of flow channel

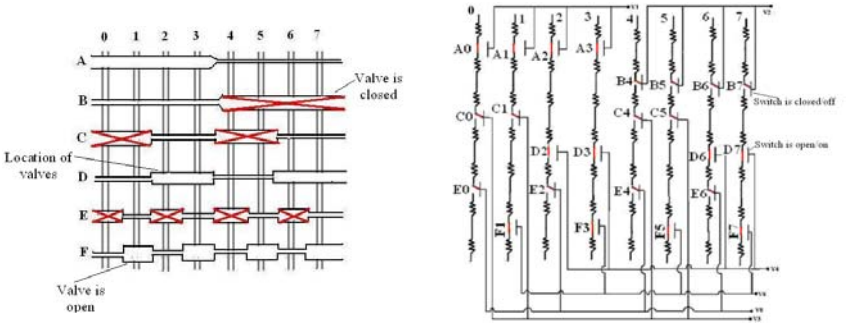

(a) (b)

FIGURE 18.13. (a) Microfluidic system consisting of "control channels" (left to right) and "flow channels" (top to bottom). Intersections with wider control channels denote valves or switches. A cross indicates a closed valve. For further details refer to (Thorsen et al., 2002). (b) The fluidic circuit representation of the system. The valves are modeled as electrical switches.

0 and control channel A is designated as "A0." Such a designation is later used to explain the circuit representation of the system. The configuration shown in Figure 18.13(a) consists of simple "on–off" valves, which can be considered as fluidic switches to control the flow in the "flow" channels. Each control line can actuate multiple valves simultaneously. Since the dimension of the control line can be varied, it is possible to have a control line pass over multiple flow channels to actuate multiple valves. The active element is the roof of the flow channel, and the intersections that act as valves or fluidic switche, are denoted by a wider width of the control channel. The intersections that are marked by a cross (Figure 18.13(a)) indicate a closed (or off) position, and the intersections that are not marked by any cross indicate an open (or on) position.

The circuit representation for the microfluidic system shown in Figure 18.13(a) (Thorsen et al., 2002) is depicted in Figure 18.13(b). Since the flow is pressure-driven, only the fluidic circuit needs to be considered. The fluidic circuit represents the flow layer, and the intersections with valves are shown as electrical switches. The resistances (or conductances) in the fluidic circuit of Figure 18.13(b) are the fluidic resistances of the channels in the flow layer. The "on–off" position of the valves depends on the gauge pressure in the control channel compared to the pressure in the flow channel. Thus, the control layer is represented in the fluidic circuit through its gauge pressure. In Figure 18.13(b) the pressure difference of the ith control channel is represented by "Vi". The notation "V" is used because of the analogy between electrical voltage and pressure. The "on" position of a switch (in Figure 18.13(b)) is represented by a vertical dash connecting two consecutive resistances (e.g., "A0"), and the "off" position of a switch

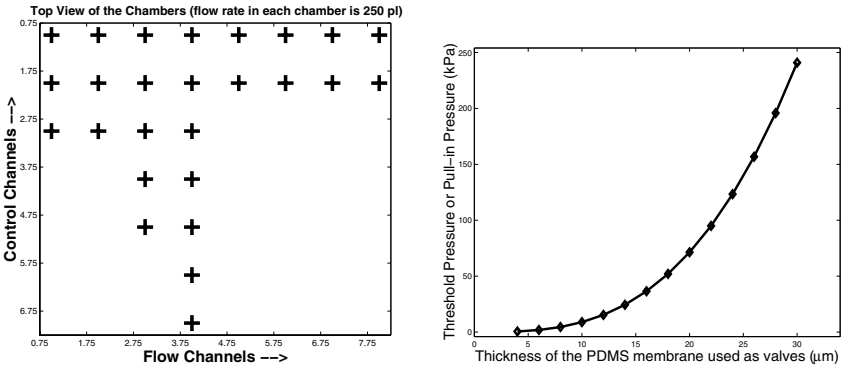

(a) (b)

FIGURE 18.14. (a) Simulation of fluid flow through the microfluidic system shown in Figure 18.13(a). The plus signs indicate presence of flow. (b) Variation of the threshold pressure with the thickness of the membrane.

is represented by a slanted dash causing a break between two consecutive resistances (e.g., "B4"). The hydraulic conductances (or hydraulic resistances) can be modeled using the approach explained in Section 18.1.2. The pressure-actuated control valves can be modeled as switches, which are considered "off" if the pressure in the control channel is above the "threshold pressure" and are considered "on" if the pressure in the control channel is below the threshold pressure. The threshold pressure can be computed from the expression (Timoshenko and Woionowsky-Krieger, 1959)

$$P_{\text{threshold}} = \frac{(\frac{ha}{2})}{(\frac{4a^4}{\pi^5 D_r} \sum_{m=1,3,5\ldots}^{\infty} \frac{(-1)^{\frac{m-1}{2}}}{m^5} \frac{\sin(\frac{m\pi}{2})}{\frac{m\pi}{a}} \{1 - \frac{\alpha_m \tanh(\alpha_m)+2}{2\cosh(\alpha_m)}\})},$$

where h is the height of the flow channel, a and b are the dimensions of the rectangular membrane acting as the valve, D_r and α_m are as defined in Section 18.1.2. Figure 18.14(a) shows the simulated flow distribution in the flow layer of the microfluidic circuit shown in Figure 18.13(b). A plus sign corresponding to a given flow channel indicates that the flow is "on;" otherwise, the flow is "off." A cell associated with a given flow channel will receive fluid only if the flow is on. Figure 18.14(b) shows the nonlinear variation of the threshold pressure with the thickness of the membrane, and Figure 18.15(a) shows the nonlinear variation of the threshold pressure with the dimension of the square membrane. Thus, for a specified threshold pressure one can choose the thickness of the membrane from Figure 18.14(b) and the dimension of the membrane from Figure 18.15(a). The CPU time to simulate the flow distribution for the system shown in Figure 18.13(a) was 16 seconds. Figure 18.15(b) shows the simulation result for an array

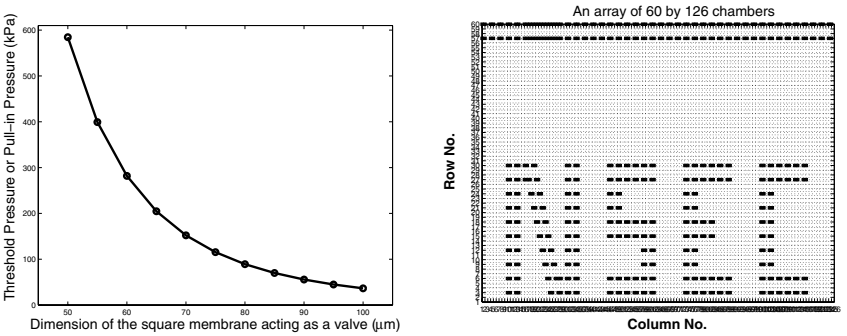

(a) (b)

FIGURE 18.15. (a) Variation of the threshold pressure with the width of the square membrane. (b) An example of large-scale integration, where the fluid is stored in a desired pattern in a microfluidic chip containing 60×126 chambers.

of 60×126 chambers. Fluid is stored in the chambers based on the filling mechanism described in Figure 18.13(a) (Thorsen et al., 2002). This result demonstrates that the fluid can be stored in any arbitrary pattern using large-scale integration of micro/nanochannels.

Lab-on-a-Chip

In the final example we consider a lab-on-a-chip system (Figure 18.16), which is designed based on the "nanochip" reported in (Becker and Locascio, 2002). The various chemical species are transported to the different modules on the chip from their sources by electrokinetic transport. One-third of the channels (marked as set A1 in Figure 18.16) perform the dual role of fluid transport and passive mixing. Each channel in the set marked as A1 is designed as shown in Figure 18.17(a) (Kutter, 2000). In this design, the characteristic dimension at a given level is half of that at the previous level. As a result, in the case of diffusion-dominated mixing, the equilibration time for mixing decreases at every level, since the equilibration time for homogeneous mixing is proportional to the square of the characteristic dimension; see Chapter 9. Thus, the homogeneity of the sample being transported increases. Figure 18.17(b) shows the circuit model, where the number of split levels used is three. In the simulations presented here, the number of splitting levels is considered as a design parameter. Figures 18.18(a) and 18.18(b) show the dependence of the flowrate and the homogeneity of the mixture, e_{mix}, on the number of split levels. The mixing

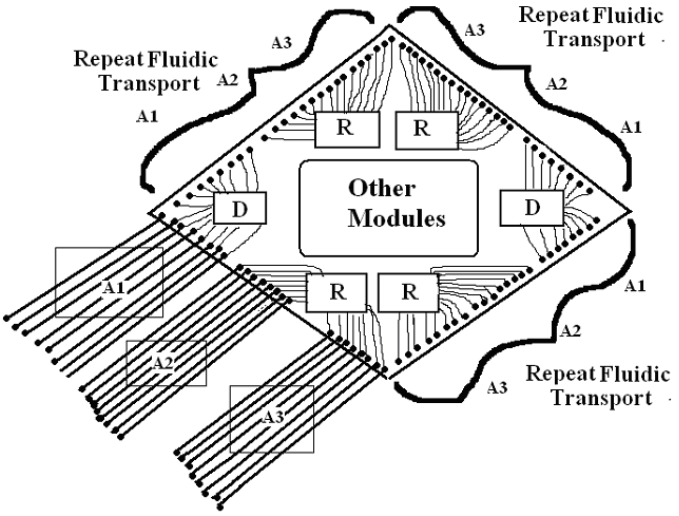

FIGURE 18.16. The schematics of the microfluidic chip considered in the lab-on-a-chip example. The fluidic transport system represented on the southwest side of the chip is duplicated on all the other sides.

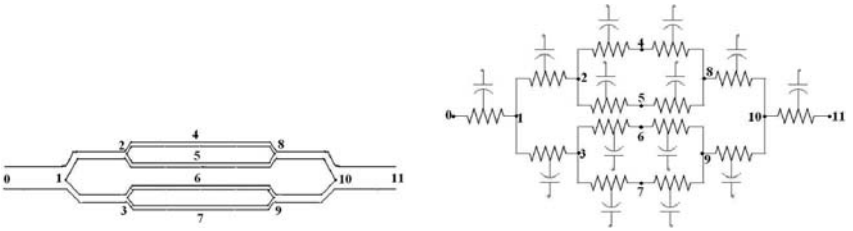

(a) (b)

FIGURE 18.17. (a) The split channel design used for fluid transport in set A1 of the microfluidic chip. This type of channel serves a dual purpose of transporting and mixing. (b) The circuit (both fluidic and electrical) representation for the split channel design.

effectiveness is defined as (see Section 9.4)

$$e_{\text{mix}} = 1 - \frac{\sqrt{\frac{1}{N}\sum_{i=1}^{N}\left(c_i - c_i^{\text{PM}}\right)^2}}{\sqrt{\frac{1}{N}\sum_{i=1}^{N}\left(c_i^0 - c_i^{\text{PM}}\right)^2}},$$

where c_i is the concentration at the ith node, c_i^{PM} is the concentration at the ith node if the two streams (i.e., the sample and the buffer streams)

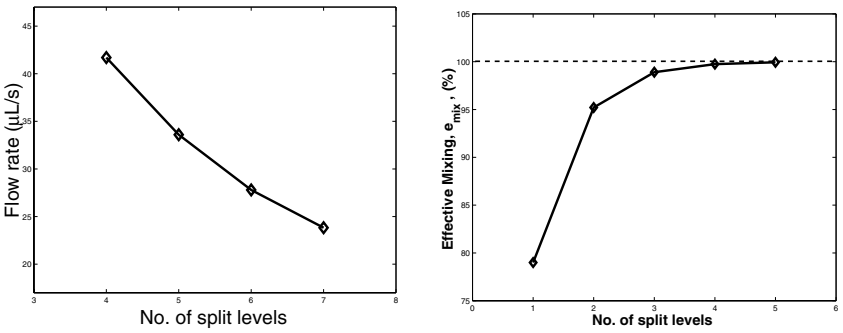

(a) (b)

FIGURE 18.18. (a) The dependence of the flowrate on the number of split levels used. (b) The dependence of the effectiveness of the mixing (i.e., homogeneity of the mixture) on the number of split levels used.

are perfectly mixed, and c_i^0 is the concentration at the ith node if the two streams do not mix at all. The analytical solution of the diffusion equation, obtained by the method of separation of variables, provides the concentration variation in the transverse direction. The mixing effectiveness, e_{mix}, ranges from 0 to 1, with 1 indicating complete mixing and 0 indicating no mixing.

The following parameters have been used for the results shown in Figures 18.18(a–b): $\Delta\phi = 100$ V (the potential difference applied between the start and the end of the channel, e.g., in Figure 18.17(a) it is applied between 0 and 11); length of each level = 200 μm; height of the initial channel = 16 μm; $\sigma_T = 6.2 \times 10^{-3}$ C/m^2; $\mu = 10^{-3}$ kg/m.s; $\epsilon = 6.95 \times 10^{-10}$. The concentration of species A at the inlet of the transport system is considered to be 0.1 mM. The results in Figures 18.18(a–b) indicate that there is a trade-off between the throughput and mixture homogeneity. However, if one uses a high value for the fluidic resistance of the initial channel, then that dominates the total fluidic resistance. As a result, the throughput is standardized and does not depend strongly on the number of splitting levels. Therefore, the device designer can control the effectiveness of the mixing process by varying the number of splitting levels.

Electrophoretic separation and electrokinetic transport are the governing mechanisms through the set of channels marked as A2 in Figure 18.16, while electrokinetic transport is the governing mechanism through the set of channels marked as A3. The species in set A1 (say A) is transported to the detection module (D), where it reacts with species B (already present in the detection chamber) to produce species C which can be used for off-chip detection. The reaction model given in Section 18.1.3 has been used to simulate the reaction between species A and B to produce species C. The initial condition corresponds to zero moles of A and C and one

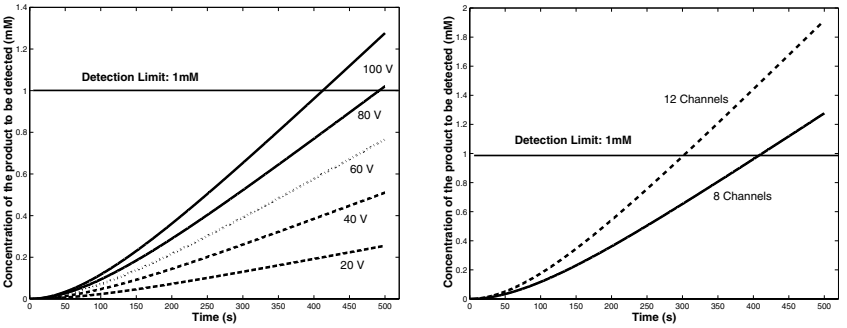

FIGURE 18.19. (a) Concentration (of species C) versus time for various applied potentials. (b) Concentration (of species C) versus time for two different numbers of input ports per side of the microfluidic chip.

mole of species B in the reaction chamber (D). A second-order forward reaction is considered for this reaction chamber (i.e., D). Therefore, the backward reaction rate is considered to be zero. A forward reaction rate of 10^{-2} $(\text{mM.s})^{-1}$ has been considered. Figures 18.19(a), 18.19(b), and 18.20(a) show the variation in the rate of formation of species C with time for different design parameters (e.g., applied potential, number of input ports per side of the chip, channel length). If the minimum concentration of species C required for detection is known (say 1 mM as considered in this case), then one can predict the detection time from the simulation results or one can design the chip to meet a specific detection time. The chemical species (G and H) transported through the channels A2 and A3 are transported to the reactor module (R in Figure 18.16), where they undergo a second-order reversible chemical reaction to produce another chemical species, F. The reaction model given in Section 18.1.3 has been used for simulating the reaction between species G and H to produce species F. The initial condition corresponds to zero moles of G, H and F in the reaction chamber (R). The following parameters have been used for this phase: total length of a single channel = 2 mm; height of a single channel = 1 μm; $\sigma_T = 2 \times 10^{-1}$ C/m^2; forward reaction rate = 0.1 $(\text{mM.s})^{-1}$; backward reaction rate = 0.01 s^{-1}. The concentration of species G at the inlet of the transport system is considered to be 20 mM and the concentration of species H is considered to be 50 mM. Figures 18.20(b) and 18.21(a) show the effect of various design parameters on the variation of the concentration of F with time. Figure 18.21(b) shows the dependence of the separation ratio (taking place in the set "A2") on the ratio of the electrophoretic mobility of the species being separated. The applied potential difference is 100 V for this case. A time step of 0.1 second has been used for this case. The CPU time to do a transient analysis of the complete system (shown in Figure 18.16) for

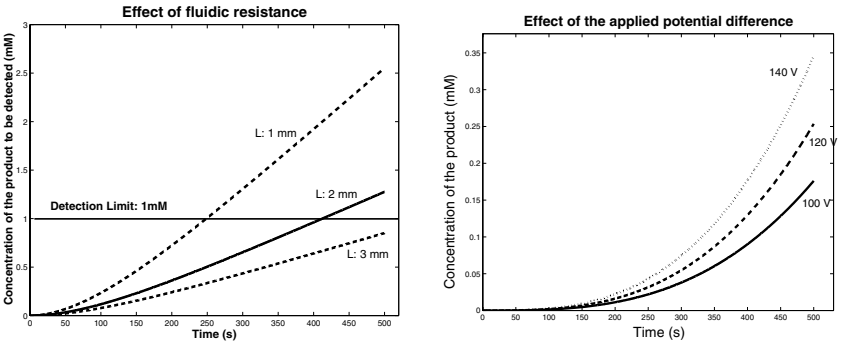

(a) (b)

FIGURE 18.20. (a) Concentration (of species C) versus time for different lengths (total) of the microfluidic channel. (b) Concentration (of species F) versus time for various applied potentials.

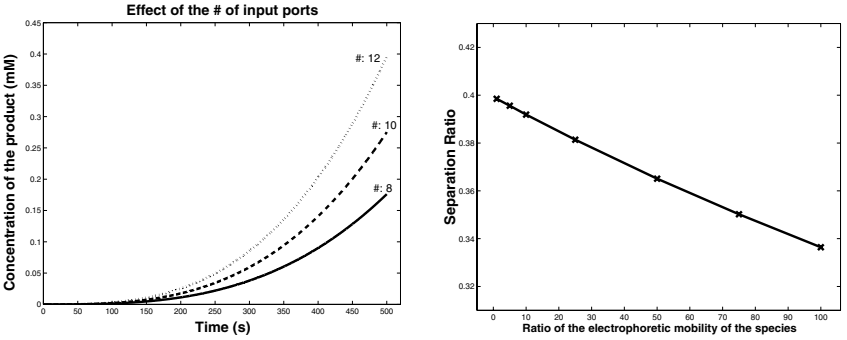

(a) (b)

FIGURE 18.21. (a) Concentration (of species F) versus time for different numbers of input ports per side of the microfluidic chip. (b) The dependence of separation ratio (taking place on set "A2" in Figure 18.16) on the ratio of the electrophoretic mobility of the species being separated.

500 seconds was on the order of 10 minutes on a PC of modest capability.

18.2 Macromodeling of Squeezed Film Damping

The dynamical behavior of microsystem components is often strongly affected by viscous air damping effects. They have to be carefully taken into account during the design and optimization process in order to get a realistic and reliable description of the device operation. The damping effects

can be treated in two ways. The first is as a damping coefficient in the simulation model at the descriptional level (e.g., mechanical FEM device model or system-level compact model) as a fit parameter. The other method is to accurately treat it using a physical model (on the continuous-field level by solving the Navier–Stokes equations), which implies a large computational effort. The first method is easy. However, it lacks physical transparency, whereas the second method becomes prohibitive in the case of complex device geometry and/or coupling with other physical energy domains. However, for a large class of MEM devices, we can use a simplified form of the Navier–Stokes equations, e.g., the Reynolds squeezed film equation, which requires considerably less computational cost. Reynolds squeezed film equation (see Section 6.1) is typically applicable when a small gap between the two plates/structures opens and closes with time. This assumption holds for structures where the seismic mass moves perpendicular to a fixed wall, for plates with tilt around horizontal axes, and for clamped beams where the flexible part moves against a fixed wall. Some examples of MEM devices where the Reynolds equation is valid are fixed–fixed beams, cantilever beams, and micromirrors.

The nonlinear isothermal compressible Reynolds squeezed film equation for air damping with slip flow is (see Section 6.1)

$$\nabla \cdot \left[(1 + 6\,\mathrm{Kn})h^3 p \nabla p\right] = 12\mu \frac{\partial(ph)}{\partial t},$$

where $h(x, y, t)$ is the variable gap between the movable part and the ground electrode of the MEM device, $p(x, y, t)$ is the air pressure under the beam, $\mathrm{Kn}(x, y, t) = \lambda/h$ is the Knudsen number, where λ is the mean free path of air. Figure 18.22 shows a typical MEM device, a deformable beam/plate at a height $h(x, y, t)$ over a ground plane, which in the undeformed state is the initial gap between beam and the ground plane. The shaded region (on the xy plane) is the domain where the Reynolds equation is solved with the boundaries indicated in Figure 18.22. Depending on the example considered, the boundary conditions can change. For a mirror, the fluid system is assumed to be open (ambient pressure) on all sides, whereas for a fixed–fixed beam, the fluid system is open along the sides of the beam and closed (no flow) at the ends of the beam. Squeezed film damping in MEMS is a coupled phenomenon (mechanics, electrostatics, and fluidics). In order to obtain a self-consistent solution at any time instant, an iterative scheme has to be followed (e.g., a relaxation scheme) among the three domains. Considerable amount of work has been done in the reduced-order modeling of squeezed film damping in MEMS. They fall into the categories already discussed in Chapter 17, namely, equivalent circuit models, Galerkin methods, description language models/mixed-level simulation, and black box models.

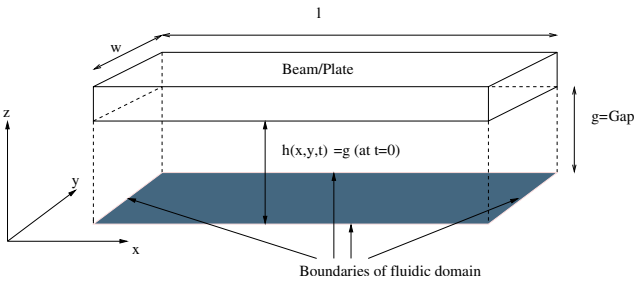

FIGURE 18.22. Domain for solving squeezed film damping equation in a MEM device.

18.2.1 Equivalent Circuit Models

Compact models for squeezed film damping based on equivalent circuit representation have the advantage of being incorporated into standard circuit simulators. The forces created by a squeezed gas film between vertically moving planar surfaces can be divided into spring and damping forces, which can be realized with frequency-dependent resistors and inductors (Veijola et al., 1995a). The second-order nonlinear Reynolds equation can be linearized when the motion of the plate(s) is small, the two plates are substantially parallel, and the motion is perpendicular to the surface of the plates. The linearized equation is written as

$$\frac{p_0 g^2}{12\mu_e}\nabla^2\left(\frac{p}{p_0}\right) - \frac{\partial}{\partial t}\left(\frac{p}{p_0}\right) = \frac{\partial}{\partial t}\left(\frac{x}{g}\right), \tag{18.13}$$

where p is a small pressure change of the static pressure p_0. The variation of the plate spacing x is also assumed to be small compared with the static gap g; μ_e is the effective viscosity of the gas given by (Veijola et al., 1995a)

$$\mu_e = \frac{\mu}{1 + 9.638\mathrm{Kn}^{1.159}}.$$

The linearized Reynolds equation (18.13) has two principal components in its solution, one in phase with the plate movement and the other out of phase, i.e., the spring term and the damping term, respectively. The force components can be calculated by integrating over the plate area, which for a rectangular plate is given (Blech, 1983) as an infinite series expansion

$$\frac{F_0}{x} = \frac{64Sp_0A}{\pi^6 g}\sum_{m,n(\mathrm{odd})}\frac{m^2 + c^2n^2}{(mn)^2[(m^2 + c^2n^2) + S^2/\pi^4]}, \tag{18.14}$$

$$\frac{F_1}{x} = \frac{64S^2p_0A}{\pi^8 g}\sum_{m,n(\mathrm{odd})}\frac{1}{(mn)^2[(m^2 + c^2n^2) + S^2/\pi^4]}, \tag{18.15}$$

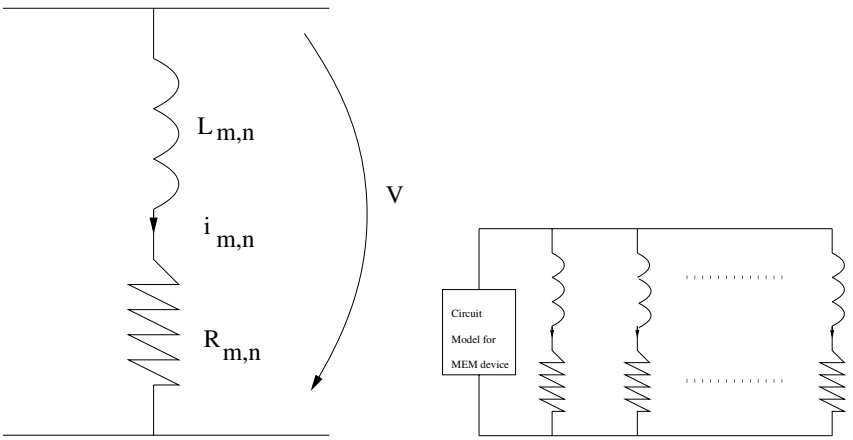

FIGURE 18.23. (a) Equivalent circuit element for squeezed film damping. (b) Equivalent circuit for squeezed film damping in the entire gap.

where m and n are odd integers, $A = WL$ is the plate area, and $c = W/L$. Here W and L are the width and length of the mass planar surfaces as shown in Figure 18.22; S is the squeeze number given by

$$S = \frac{12\mu_e W^2}{p_0 g^2}\omega,$$

and ω is the angular frequency. The forces in equations (18.14), (18.15) can be represented by the electrical equivalent circuit using a combination of an inductance (equals the spring behavior of the gas) and a resistance (acts as a damping element) in series, as shown in Figure 18.23(a). Figure 18.23(a) shows a single element for a corresponding m and n. The actual equivalent circuit for squeezed film damping would consist of a parallel combination of such elements (for various m and n) connected in parallel to the MEM device circuit as shown in Figure 18.23(b). The governing differential equation for the circuit shown in Figure 18.23(a) is

$$L_{m,n}\frac{\partial i_{m,n}}{\partial t} + R_{m,n} i_{m,n} = V = \frac{\partial u}{\partial t}, \tag{18.16}$$

where V is the voltage drop through the element (analogous to velocity in mechanics and represented by the flux term $\frac{\partial u}{\partial t}$). At steady state (all signals are sinusoidal having a single angular frequency ω), the current and velocity (flux term) can be expressed as

$$i_{m,n} = I_{m,n}\exp(j\omega t), \qquad u = U\exp(j\omega t),$$

where I and U are complex coefficients. Putting this in equation (18.16), we get

$$I_{m,n} = \frac{j\omega}{R_{m,n} + j\omega L_{m,n}} U,$$

and hence the total current in the squeezed film equivalent circuit that corresponds to the total force is the sum of all currents of the parallel sections

$$I_s = \sum_{m,n(\text{odd})} I_{m,n} = U \sum_{m,n(\text{odd})} \frac{j\omega}{R_{m,n} + j\omega L_{m,n}}.$$

The imaginary and the real parts of the ratio I_s/U are

$$Im\left(\frac{I_s}{U}\right) = \sum_{m,n(\text{odd})} \frac{R_{m,n}\omega}{R_{m,n}^2 + \omega^2 L_{m,n}^2}, \qquad \text{Re}\left(\frac{I_s}{U}\right) = \sum_{m,n(\text{odd})} \frac{L_{m,n}\omega^2}{R_{m,n}^2 + \omega^2 L_{m,n}^2},$$

which satisfy the frequency dependency specified in equations (18.14), (18.15), respectively. This requires that $Im\left(\frac{I_s}{U}\right) = F_0/x$ and $\text{Re}\left(\frac{I_s}{U}\right) = F_1/x$. This gives

$$L_{m,n} = (mn)^2 \frac{\pi^4 g}{64 A p_0}, \qquad R_{m,n} = (mn)^2 (m^2 + c^2 n^2) \frac{\pi^6 g^3}{768 A W^2 \mu_e}.$$

The components $L_{m,n}$ and $R_{m,n}$ depend on the distance g (the static gap). If the displacement is large, the component values will also vary with the displacement and hence are nonlinear in nature. The equivalent circuit of squeezed film damping is connected in parallel with the MEM device circuit, and the whole system can be solved using any standard circuit simulator. For more details on circuit modeling of squeezed film damping, see (Veijola, 2001; Turowski et al., 1998).

18.2.2 Galerkin Methods

Linear modes of vibration of a system have been used for reduced-order modeling of MEM dynamics as discussed in Chapter 17. In this section, squeezed film damping has been considered in such a model-order reduction. The fluid (film) in between the plates typically undergoes Stokes flow (low Reynolds number, hence negligible inertia effects) and thus does not have any "normal modes" of its own that could be used for basis functions in combination with the elastic modes. One obvious approach is to linearize the dissipative effect under an assumption of small motion. Once linearized, frequency-domain analysis can be used, converting the time-dependent dissipation problem in the time domain into a time-independent frequency-domain calculation of amplitude and phase response. This approach was the basis for the early squeezed film damping work involving rigid body motion and has been widely used in the MEMS field. Even when the moving body is flexible, it is possible to use the modal amplitude to create a

moving boundary condition for the fluidic system and calculate the reaction force. This has been done for small-amplitude damped resonant motions of flexible microbeams and resonators. When the amplitudes are large, such as for the electrostatic pull-in of a beam, linearized modal solutions are not accurate. In (Mehner et al., 2003), an approach has been presented to add dissipative effects of squeezed film damping (Reynolds equation) in the transient and harmonic analysis of MEMS. The macromodels are automatically generated by a modal projection technique based on the harmonic transfer functions of the fluidic domain. The transfer functions are either obtained at the initial position (small signal case) or at various deflection states (large deflection case). In this method, an equivalent damping and stiffness matrix that captures the true dependency between structural velocities and fluid pressure is computed in the modal coordinates. The damping $C_{ji}\dot{q}_i$ and the stiffness coefficients $K_{ji}q_i$ of such a matrix representation can be obtained from the following modal force balance equation:

$$C_{ji}\dot{q}_i + K_{ji}q_i = \phi_j^T \int N^T p(\phi_i \dot{q}_i) dA,$$

where q_i is the modal coordinate, ϕ_i is the ith eigenvector (mode), and N^T is the vector of finite element shape functions. Here C_{ji} and K_{ji} state the dependency between structural wall velocities caused by mode i and the reacting fluid forces that act on mode j. The damping and the squeeze coefficients of each mode are the main diagonal terms. Off-diagonal terms represent the fluidic crosstalk among modes, which happens in case of asymmetric gap separation. The following steps are performed to obtain the coefficients of C and K:

1. The squeezed film model is excited by wall velocities that are equal to the values of the first eigenvector (mode).

2. A harmonic response analysis is performed to compute the pressure response in the entire frequency range.

3. The real and the imaginary parts of the element pressure are integrated and the complex nodal force vector computed for each frequency.

4. The scalar product of all eigenvectors and the nodal force vector of step 3 is computed. The resulting numbers are modal forces, which indicate how much of the pressure distribution acts on each mode.

5. The damping and the stiffness coefficients are extracted from the real and the imaginary parts of the modal forces.

6. Steps 1 to 5 are repeated for each eigenmode.

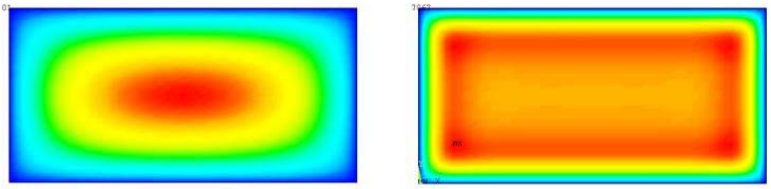

(a) (b)

FIGURE 18.24. (a) Pressure distribution under an oscillating flat plate at low frequency. (b) Pressure distribution under an oscillating flat plate at high frequency. (*http : //www.ansys.com/ansys/mems/mems_downloads/thermal_analogy_damping.pdf*)

A modal decomposition of damping effects is acceptable, since the Reynolds squeezed film equation is linear. More examples using modal basis functions for MEMS simulations are given in (Gabbay and Senturia, 1998; Varghese et al., 1999). Figure 18.24(a) shows the pressure distribution under a flat plate for a low frequency of oscillation, while Figure 18.24(b) shows the pressure distribution under a flat plate for a high frequency of oscillation. At high frequency, the fluid cannot easily escape from the sides, giving roughly uniform and high pressure under the plate.

The Karhunen–Loève decomposition method for model order reduction has also been effectively used for squeezed film damping in (Hung and Senturia, 1999). The method used is basically the same as that in the absence of damping. From a few full-simulation runs, snapshots are taken for the fluid pressure distribution and a set of pressure basis functions formed using an SVD analysis. These basis functions are then used in the dynamic simulation of the device, thereby reducing the order of the system. The nonlinear Reynolds equation can be reduced efficiently using this method with no linearization involved as in the case of the equivalent circuit representation. The trajectory piecewise-linear approach has also been used for modeling squeezed film damping in MEM devices; see (Rewienski and White, 2001), for details.

18.2.3 Mixed-Level Simulation

A mixed-level formulation uses a hardware description language for modeling squeezed film damping (Schrag and Wachutka, 2002). From an FEM model of the microstructure built by any standard FEM tool, a netlist for finite network (FN) simulation is constructed utilizing the grid and the geometric information from the FEM model. The governing equations (the Reynolds equation and the mass continuity equation) are discretized and coded in VHDL-AMS (Schrag et al., 2001; Sattler et al., 2003). The limitations of the Reynolds equation due to edge effects and perforations on the

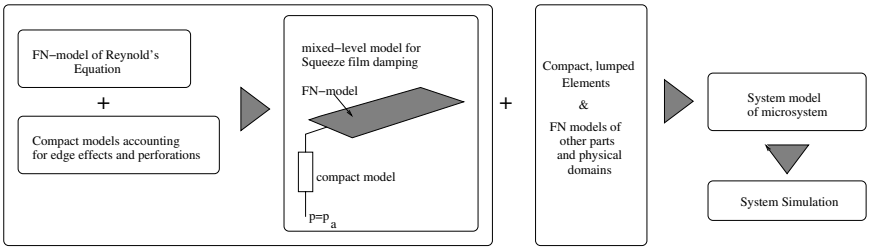

FIGURE 18.25. Mixed-level approach for modeling squeezed film damping in MEMS (see (Schrag and Wachutka, 2002), for details).

plate are rectified using error-compensating compact models. These compact models are in the form of lumped circuit elements such as resistances or constants, which can be determined from a few FEM simulations. The FN model in the sense of the Kirchhoffian network theory describes the squeezed film damping by two conjugate variables, namely, the pressure difference p_{ik} between two adjacent nodes ("across variables") and the corresponding mass flow rate Q_{ik} ("through variable") (Schrag and Wachutka, 2002). The mass balance equation is satisfied automatically as a result of the Kirchhoffian laws. However, correct formulation of the mass flowrate at each node must be done separately. The FN model can be implemented into a general-purpose system simulator and applied to arbitrary device geometries. The flowchart for the method is shown in Figure 18.25.

18.2.4 Black Box Models

The Arnoldi method has been used in (Chen and Kang, 2001a), to solve a MEMS micromirror device for both small and large deflections in the presence of fluid damping. The fluid damping equation (nonlinear isothermal Reynolds equation) has been linearized using Taylors series, and the Arnoldi method has been used to construct a reduced-order linear model for small angular deflections. For large angular deflections, both the linear and the second-order nonlinear terms from the fluid equation were retained in the Taylors expansion, and the Arnoldi method has been applied to construct a weakly nonlinear model. The accuracy can be increased by considering higher-order terms in the Taylors expansion, but the computational cost goes up, restricting the use of the process. The trajectory piecewise-linear approach overcomes some of these difficulties, as described in Chapter 17.

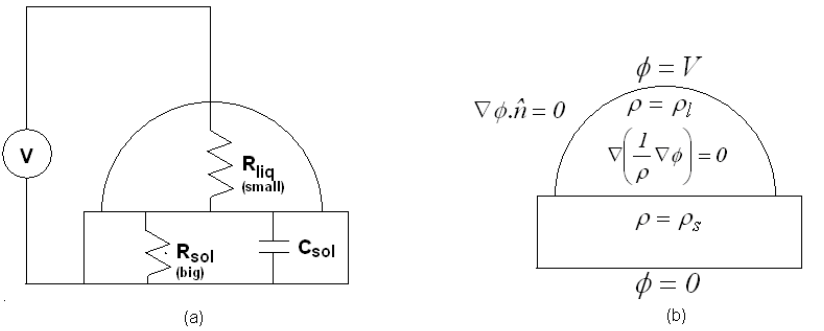

FIGURE 18.26. (a) A bulk circuit diagram for a liquid with a small amount of electrical resistance $R_{\rm liq}$ atop a dielectric solid with capacitance $C_{\rm sol}$ and a large electrical resistance $R_{\rm sol}$. (b) The corresponding steady-state PDE with boundary conditions.

18.3 Compact Model for Electrowetting

In Chapter 8, we discussed electrowetting and the associated physical phenomena. Here we revisit electrowetting and discuss a compact model. Figure 18.26(a) shows the equivalent circuit diagram for the liquid-drop-dielectric solid system. Here ϕ is the electrical potential inside the drop, and ρ_l and ρ_s are the resistivities of the liquid and solid, respectively. The total impedence for the circuit diagram shown in Figure 18.26 is (Shapiro et al., 2003a)

$$\frac{V(s)}{I(s)} = z(s) = \frac{1 + \frac{R_{\rm liq}}{R_{\rm sol}} + sR_{\rm liq}C_{\rm sol}}{sC_{\rm sol} + \frac{1}{R_{\rm sol}}},$$

where s is the Laplace variable. For a sinusoidal signal $V(t) = \tilde{V}\cos(\omega t)$ of frequency ω, s is taken as $s = i\omega$. The voltage drop across the solid $V_{\rm sol}(s)$ is given by

$$V_{\rm sol}(s) = z_{\rm sol}(s)I(s) = \frac{z_{\rm sol}(s)}{z(s)}V(s) = \left(\frac{1}{1 + \frac{R_{\rm liq}}{R_{\rm sol}} + sR_{\rm liq}C_{\rm sol}}\right)V(s).$$

In the steady state (i.e., $s = i\omega \to 0$), the voltage and energy stored in the dielectric are

$$\tilde{V}_{\rm sol} = \left(\frac{1}{1 + \frac{R_{\rm liq}}{R_{\rm sol}}}\right)\tilde{V} \quad \text{and} \quad E_{de} = \frac{1}{2}C_{\rm sol}\left(\frac{1}{1 + \frac{R_{\rm liq}}{R_{\rm sol}}}\right)^2\tilde{V}^2, \qquad (18.17)$$

where $\tilde{V}$ is the applied DC voltage. The dependence shown in equation (18.17) is similar to the energy in the perfectly insulating solid; $E_{\rm de}(R,\theta) =$

$\frac{1}{2}\frac{\epsilon_s V^2}{h}\pi R^2 \sin^2\theta$, except for the new $R_{\text{liq}}/R_{\text{sol}}$ term. Hence, the resistance of the liquid drop R_{liq} is shape-dependent. This dependence of resistance on the droplet shape gives rise to contact angle saturation in this model, see (Shapiro et al., 2003a; Shapiro et al., 2003b), for more details. The corresponding PDE and boundary conditions for the equivalent circuit diagram are shown in Figure 18.26(b).

18.4 Software

Several software packages have been developed, both commercially and by universities, for the simulation of microsystems (including microfluidic systems) using macromodels. Table 18.2 presents some of the available software packages.

TABLE 18.2. Software packages for reduced-order modeling of MEMS and microfluidics.

Name	Manufacturer	Description
HDL-A	Mentor Graphics Inc.	Analog and mixed signal analysis (equivalent circuits for MEMS/microfluidics).
MAST/SABER	Synopsys Inc.	Analog and mixed signal analysis (equivalent circuits for MEMS/microfluidics).
SpectreHDL	Cadence Design Systems	Analog and mixed signal analysis (equivalent circuits for MEMS/microfluidics).
NODAS	Carnegie Mellon Univ.	A library of parameterized components for using SABER (Synopsys Inc.) nodal simulator to simulate MEMS devices.
SPICE	U of C, Berkeley	A general-purpose circuit simulation program for nonlinear dc, nonlinear transient, and linear ac analyses (equivalent circuits for MEMS/microfluidics).
SUGAR	U of C, Berkeley	An open source simulation tool for MEMS based on nodal analysis techniques.
ANSYS Multiphysics	ANSY Inc.	Modal analysis, reduced-order models for fluid damping, system-level simulation.
MEMS Xplorer	MEMSCAP Inc.	System level simulation (Equivalent circuits for MEMS).
CoventorWare	Coventor Inc.	Macromodels and system-level models for MEMS and microfluidics.